ISPRS Annals of the Photogrammetry, Remote Sensing and Spatial Information Sciences, Volume XII-4/W2-2026
10th International Conference on Smart Data and Smart Cities (SDSC), 29 September–1 October 2026, Sofia, Bulgaria

Efficient Geometric Quality Inspection of Large-Scale Ship Components via Nap-Of-The-Object Photogrammetry

Mercedes Lo-Ting Yeh[1], Haoran Guo[1], Yansong Duan[1,*]

[1] School of Remote Sensing and Information Engineering, Wuhan University, Wuhan 430079, China
E-mails: Mercedes1222@126.com, haoran_guo@whu.edu.cn, ysduan@whu.edu.cn[*]

Keywords: Ship Components, Geometric Quality Inspection, UAV, Nap-of-the-object Photogrammetry.

Abstract

Ship components in the shipbuilding industry are often large in size and structurally complex, making it difficult for conventional quality inspection techniques to simultaneously satisfy efficiency and accuracy requirements. To address this issue, this paper proposes a geometric quality inspection method for ship components based on nap-of-the-object photogrammetry. First, a UAV flight path is planned according to the CAD design model of the target component, and a micro-UAV is used to acquire high-resolution images. High-precision 3D reconstruction is then performed by integrating exterior orientation parameters such as heading, attitude, and gimbal angle. Finally, geometric primitive fitting between the 3D reconstruction model and the CAD design model is conducted to evaluate geometric indicators including perpendicularity, parallelism, coplanarity, and detailed deviations. A segmented ship component was selected as the experimental subject. The measurement results obtained from the 3D reconstruction model were compared with the corresponding data from the CAD design model. The results demonstrate good perpendicularity, parallelism, and coplanarity, with 90% of the measurement deviations within ±5 mm, and a maximum error of 1.46 cm, confirming the feasibility of the proposed method for geometric quality inspection of ship components. As a non-contact, high-precision, and high-efficiency measurement technique, nap-of-the-object photogrammetry can significantly enhance production efficiency and product quality in the shipbuilding industry, thereby promoting its modernization.

1. Introduction

In modern shipbuilding, high-precision measurement and accuracy control are critical to ensuring construction quality and improving manufacturing efficiency (Yuzaki and Okomoto, 1993). Ocean-going vessels often weigh tens of thousands of tons and are assembled from tens of thousands of precision components. To improve efficiency, the industry widely adopts block construction, in which hull blocks are prefabricated separately and then assembled (Zhong et al., 2013). However, due to various production conditions and technological factors, deviations inevitably exist between structural components, blocks, and sections and their design models (Li et al., 2025). Consequently, measurement tasks during construction are particularly demanding. Therefore, achieving efficient and high-precision geometric quality inspection remains a persistent challenge in the shipbuilding field.

In the past, ship component measurement relied primarily on traditional tools such as steel rulers, squares, theodolites, and levels. Although these methods offer low cost and simple operation, they suffer from limited measurement range, low efficiency, and are prone to human error (Dujam et al., 2024). Total stations integrate distance and angle measurement functions, enabling rapid acquisition of three-dimensional coordinates with accuracy reaching up to 0.5 mm. However, when applied to complex irregular ship components requiring dense point measurements, total stations face considerable challenges (Maisano et al., 2023). Three-dimensional laser scanning can rapidly acquire dense point clouds, but post-processing for complex irregular components is complicated, and specular reflection on smooth surfaces can lead to measurement failure (Wang and Feng, 2016). As a result, researchers have turned to image-based photogrammetry. For instance, Niebylski (Niebylski, 2025) implemented both analog and digital photogrammetry for online measurement control in ship hull assembly. Faizin et al. (Faizin et al., 2024) employed photogrammetry to reconstruct three-dimensional boat propeller blades and compared the accuracy of Agisoft Metashape and artificial intelligence (AI)-based methods against coordinate measuring machine (CMM) measurements. Kim et al. (Kim et al., 2024) proposed a multi-stereo three-dimensional measurement method for large-scale structures, achieving millimeter-level accuracy through an improved calibration algorithm. However, close-range photogrammetry struggles to cover large ship components comprehensively, resulting in numerous blind spots and hindering high-precision measurement.

In view of these limitations, photogrammetry based on micro-UAVs has emerged. This approach enables photography from arbitrary positions, facilitating comprehensive coverage of ship components and acquisition of high-resolution images. Combined with high-precision 3D reconstruction, it promises a novel and efficient method for geometric quality inspection of ship components.

A primary challenge in using micro-UAVs for geometric quality inspection of complex irregular ship components is obtaining comprehensive high-resolution imagery—essentially a path planning problem. Chai et al. (Chai et al., 2022) proposed a multi-strategy fusion differential evolution algorithm for three-dimensional UAV path planning in complex environments. Zhang et al. (Zhang et al., 2024) developed the RFA-Star algorithm, which employs a feature attention mechanism to identify obstacle feature points for UAV path planning in environments with high obstacle density. Ahmed et al. (Ahmed et al., 2024) introduced an energy-efficient multi-UAV multi-region coverage path planning approach that utilizes a back-and-forth pattern with Bezier curve-based smoothing turns and region allocation, thereby minimizing overall energy consumption. Due to factors such as complex ship component structures, coarse initial point clouds, complex environments, and coordinate registration errors, traditional path planning methods are difficult to apply directly (Jones et al., 2023, Liu et al., 2022, Bao et al., 2023). On the other hand, modern ship component manufacturing typically involves CAD design models that accurately describe component structures and the spatial distribution of parts (Son and Nam, 2022). This geometric information can guide path planning for micro-UAVs. Combined with UAV gimbal attitude control and high-precision RTK positioning, this approach holds promise for acquiring comprehensive high-resolution imagery.

Once such imagery is acquired, the next challenge is how to use it for geometric quality inspection. Raw images are two-dimensional information carriers and are affected by camera field of view, lens distortion, occlusion, and uneven illumination, making direct high-precision measurement difficult (Iglhaut et al., 2019). To overcome this limitation, researchers have explored image-based 3D reconstruction techniques. For instance, Chengtao Li et al. (Li et al., 2022) completed 3D reconstruction of large construction sites by equipping UAVs with CORS RTK. Chen et al. (Chen et al., 2025) provided a comprehensive review of UAV-based 3D reconstruction technologies for landslide disasters, covering sensors, reconstruction methods, and their applications in monitoring and assessment. Rodríguez-Lira et al. (Rodríguez-Lira et al., 2025) reviewed deep learning-based 3D reconstruction from images, identifying multi-view stereo and monocular depth estimation as the prevailing approaches. Image-based 3D reconstruction technology is now relatively mature. By combining it with multi-source data such as UAV RTK positioning and gimbal attitude, high-precision 3D models of ship components can be reconstructed and compared with design data to achieve geometric quality inspection.

To address the challenge of geometric quality inspection for complex irregular ship components using micro-UAVs, this paper proposes a method based on nap-of-the-object photogrammetry. The method first plans the flight path based on the CAD design model of the ship component and acquires high-resolution images using a UAV. A high-precision 3D reconstruction model is then generated by integrating exterior orientation parameters such as heading, attitude, and gimbal angle. Finally, quality inspection is performed by comparing the measurement results from the 3D reconstruction model with the CAD design model.

2. Methodology

The technical workflow of the proposed ship component quality inspection method is illustrated in Figure 1. This workflow consists of three core stages: image acquisition, 3D reconstruction, and geometric quality inspection.

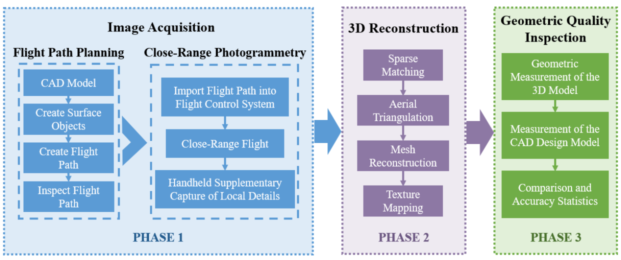

Figure 1. Technical workflow of ship component quality inspection based on nap-of-the-object photogrammetry

2.1 Image Acquisition

The core of image acquisition is flight path planning. Continuous waypoints and photography directions provide essential parameters for the flight control system, ensuring that the UAV captures comprehensive high-resolution imagery. Figure 2 illustrates the basic workflow of image acquisition, which mainly consists of photography design and flight path planning. The selection of waypoints and photography directions must satisfy the requirements of the 3D reconstruction process regarding coverage, image overlap, and reconstruction accuracy to obtain high-quality image data. Meanwhile, the organization of flight strips must comply with flight control constraints such as minimum baseline and minimum distance, ensuring that the generated flight path is connected, collision-free, and globally shortest.

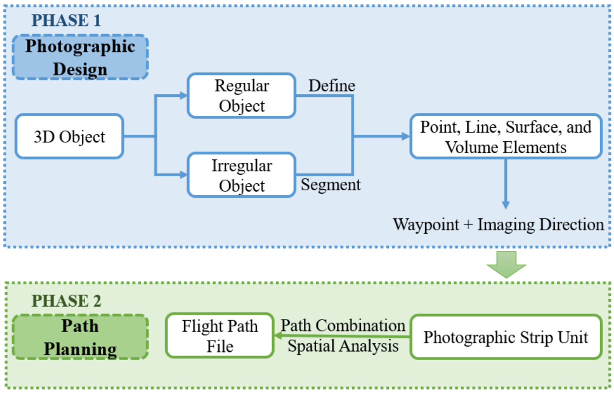

Figure 2. Technical workflow of image acquisition

2.1.1 Photography Design: Photography design is based on the initial point cloud or model of the target object. For ship components, the CAD design model can be used directly. This model represents a regular object, and based on its bounding box, the component can be subdivided into three surface types: horizontal, vertical, and inclined. Different path planning strategies are adopted for each type.

For horizontal surfaces, traditional photogrammetric methods are followed to ensure comprehensive and efficient coverage.

For vertical surfaces, a vertical rectangular face is taken as an example. The planning process and parameters are shown in Figure 3.

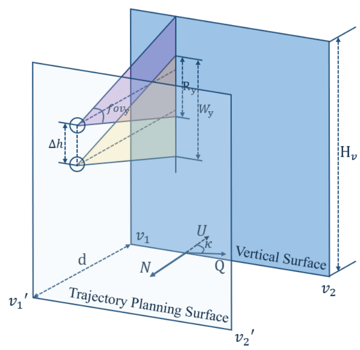

Figure 3. Schematic diagram of flight path planning for vertical surfaces

First, the spatial position and orientation of the trajectory planning surface are determined based on the coordinates of the bottom edge vertices of the model facade and the horizontal component of its normal vector. As shown in Figure 3, let the bottom edge vertices of the model facade be (v_1, v_2), the horizontal unit component of the normal vector be $\mathbf{N}(x, y)$, and the facade height be H_v. Translating the model facade along $\mathbf{N}$ by a distance d yields a plane with bottom edge vertices (v_1', v_2'), which is defined as the trajectory planning surface. The translation distance d is determined by the camera focal length f, pixel size p, and ground sampling distance (GSD), and is expressed as:

$$d = \frac{f}{p} \cdot \text{GSD} \tag{1}$$

The spatial coordinates and imaging directions of each waypoint are then determined. This study adopts the North-East-Down (NED) coordinate system to define UAV attitude, as illustrated in Figure 4. The yaw angle κ is defined as the angle from true north to the UAV nose direction, with clockwise rotation positive and counterclockwise negative, ranging from $-180°$ to $180°$. The pitch angle ϕ is defined as the tilt angle of the camera lens, with downward rotation negative, ranging from $-90°$ to $0°$.

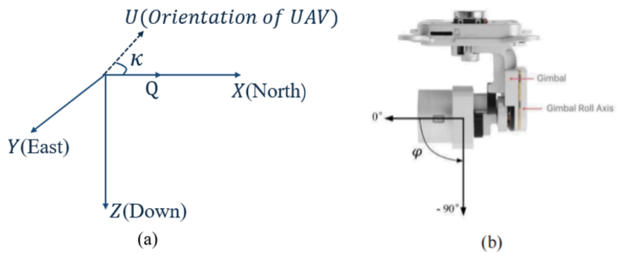

Figure 4. Schematic diagram of yaw angle κ and pitch angle ϕ

During flight, the UAV fuselage must remain perpendicular to the measured facade, i.e., oriented opposite to the normal vector $\mathbf{N}$. Let the north-pointing unit vector pointing north be $\mathbf{Q} = (1, 0)$ and the target direction vector be $\mathbf{U} = -\mathbf{N}$. The yaw angle κ corresponds to the signed angle required to rotate from $\mathbf{Q}$ to $\mathbf{U}$, which can be computed as:

$$\kappa = \text{atan2}(\mathbf{Q} \times \mathbf{U},\ \mathbf{Q} \cdot \mathbf{U}) \tag{2}$$

Here, $\mathbf{Q} \times \mathbf{U} = Q_x U_y - Q_y U_x$ is the two-dimensional cross product. It yields a scalar value, and its sign indicates the direction of rotation. $\mathbf{Q} \cdot \mathbf{U} = Q_x U_x + Q_y U_y$ is the dot product, reflecting the cosine of the included angle. According to the definition of the $\text{atan2}(y, x)$ function, this expression directly yields the signed angle κ from $\mathbf{Q}$ to $\mathbf{U}$.

When $\phi = 0°$, vertical photography of the facade is achieved. When designing left and right convergent flight strips, κ can be adjusted accordingly. When designing downward convergent strips, ϕ can be appropriately reduced.

Taking the top-left corner point on the trajectory planning surface as the starting waypoint, the coordinates of the remaining waypoints can be sequentially calculated based on the horizontal spacing Δs and vertical spacing Δh between adjacent waypoints.

The horizontal spacing Δs is determined by the horizontal field of view and the forward overlap rate. Let the horizontal field of view be fov_x. The horizontal coverage width of a single image is:

$$W_x = 2d \cdot \tan\left(\frac{\text{fov}_x}{2}\right) \tag{3}$$

Let the horizontal overlap rate be r_x. The horizontal overlap length between adjacent images is $R_x = r_x \cdot W_x$. Thus, the horizontal spacing between adjacent waypoints is:

$$\Delta s = W_x - R_x = 2d(1 - r_x) \tan\left(\frac{\text{fov}_x}{2}\right) \tag{4}$$

Similarly, the vertical spacing Δh between adjacent waypoints can be expressed as:

$$W_y = 2d \cdot \tan\left(\frac{\text{fov}_y}{2}\right) \tag{5}$$

$$\Delta h = 2d(1 - r_y) \tan\left(\frac{\text{fov}_y}{2}\right) \tag{6}$$

where fov_y is the vertical field of view and r_y is the vertical overlap rate.

Inclined surfaces can be treated as vertical surfaces rotated about their bottom edge. First, the normal vector of the inclined surface is calculated, and the surface is translated along this normal vector by the imaging distance d to obtain the trajectory planning surface. The surface is then rotated about its bottom edge by a certain angle to transform it into an equivalent vertical surface for planning. After completing the photography design for the equivalent vertical surface, the results are transformed back to the original inclined surface to obtain the actual trajectory planning results, as shown in Figure 5.

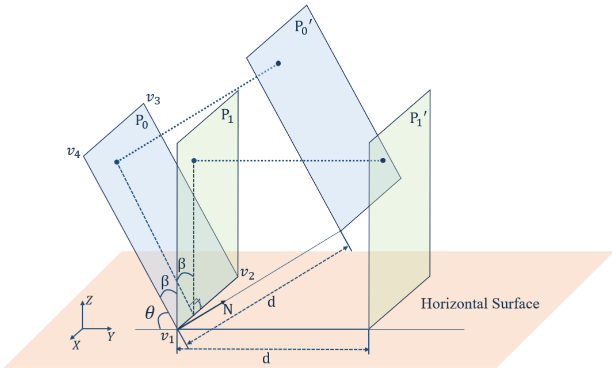

Figure 5. Schematic diagram of flight path planning for inclined surfaces

Let the inclined surface be P_0, with bottom edge vertices (v_1, v_2) and top edge vertices (v_3, v_4). Taking three non-collinear points v_1, v_2, v_3 arranged counterclockwise, the normal vector $\mathbf{N}$ of the inclined surface can be calculated as follows:

$$\mathbf{N} = (v_2 - v_1) \times (v_3 - v_1) \tag{7}$$

If the Z-component of $\mathbf{N}$ is negative, the vector is reversed to ensure it points toward the positive Z-axis.

Translating P_0 along $\mathbf{N}$ by distance d yields the trajectory planning surface P_0'. As shown in Figure 5, rotating the inclined surface about its bottom edge by $\beta = 90° - \theta$ (where θ is the acute angle between P_0 and the horizontal plane) yields its equivalent vertical surface P_1, for which path planning is performed as for vertical surfaces.

Finally, the waypoints on the equivalent trajectory planning surface P_1' are rotated about the axis through v_1 with direction $\langle v_1, v_2 \rangle$ by $-\beta$ to obtain the waypoints on P_0'. The camera rotation angle at each waypoint is increased by $-\beta$ to obtain the final trajectory planning results for the inclined surface.

2.1.2 Path Planning Maintaining a constant altitude during flight reduces power consumption and increases endurance. Therefore, the proposed method selects the horizontal direction as the main flight direction, varying altitude to cover the target surface in a serpentine pattern, as shown in Figure 6(a). To improve imaging direction accuracy and eliminate blind spots, convergent flight strips can be added, as illustrated in Figure 6(b).

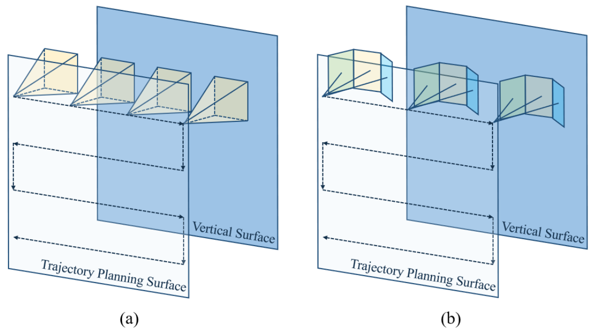

Figure 6. Path planning for vertical surfaces: (a) orthographic flight strips; (b) convergent flight strips

For horizontal surfaces, conventional photogrammetric path planning is adopted.

To ensure flight safety, the flight path should be adjusted based on the minimum safe flight altitude and ground obstacles. To capture lower parts of the object below the minimum safe altitude, additional paths with the camera tilted downward can be added near the bottom of the vertical surface.

The generated flight path file is then imported into the UAV to perform nap-of-the-object photogrammetry on each target surface. To ensure sufficient redundancy for 3D reconstruction, the forward overlap rate is set to no less than 80%, and the side overlap rate to no less than 60%. After image acquisition, images with low positioning accuracy, motion blur, or significant occlusion are removed, resulting in a high-quality image dataset for subsequent processing.

2.2 3D Reconstruction

After acquiring high-resolution images and shooting parameters, modeling can be accomplished using established 3D reconstruction techniques. Figure 7 illustrates the technical workflow.

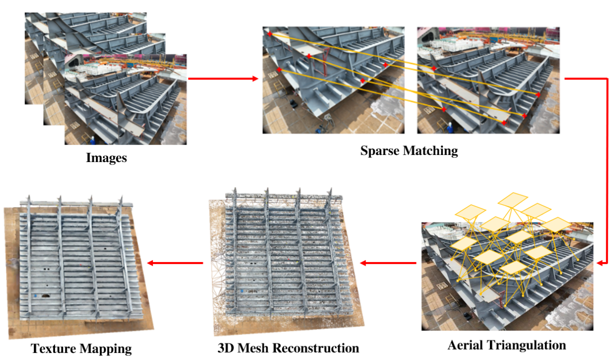

Figure 7. Workflow of 3D reconstruction

To ensure the accuracy of the 3D reconstruction model, the SIFT operator is used for sparse matching to enhance the robustness of feature point extraction and matching. A high-precision total station is used to measure uniformly distributed typical feature locations as control information, including control points and checkpoints. Bundle adjustment is then applied for aerial triangulation to obtain interior and exterior orientation parameters. The Multi-View Stereo (MVS) algorithm is used for dense reconstruction, and Poisson surface reconstruction is used to generate a 3D mesh from the dense point cloud. Finally, smoothing optimization and texture mapping are performed to obtain a high-precision nap-of-the-object 3D model.

2.3 Geometric Quality Inspection

After high-precision 3D reconstruction, geometric quality inspection can be performed on the nap-of-the-object model. To quantitatively evaluate the consistency between the 3D reconstruction model and the CAD design model in terms of macroscopic geometric morphology, this study proposes a geometric quality inspection method based on geometric primitive fitting. Using the CAD design model as a reference, corresponding key point coordinates and bidirectional point distances are measured on the 3D reconstruction model. Straight lines representing key geometric features are fitted, and the perpendicularity and coplanarity of ship component details are examined to assess geometric accuracy.

For corresponding points on the same edge, the least-squares spatial line fitting method is used. Let the point set be $\{P_i\}$. The fitted line is represented by a direction vector $\mathbf{v}$ and a point $\mathbf{P}_0$ on the edge. The direction vector is obtained from the eigenvector corresponding to the largest eigenvalue of the covariance matrix, solving:

$$\mathbf{M} = \frac{1}{n}\sum_{i=1}^{n}(P_i - \bar{P})(P_i - \bar{P})^T \tag{8}$$

where $\bar{P}$ is the centroid of the point set, and $\mathbf{v}$ is the eigenvector corresponding to the largest eigenvalue of $\mathbf{M}$.

To examine whether the reconstructed model preserves the angular relationships in the CAD design, the angles between fitted lines in the 3D reconstruction model are calculated and compared with the theoretical angles in the CAD model. For two lines with direction vectors $\mathbf{v}_1'$ and $\mathbf{v}_2'$, the angle is:

$$\theta' = \arccos\left(\frac{|\mathbf{v}_1' \cdot \mathbf{v}_2'|}{\|\mathbf{v}_1'\|\|\mathbf{v}_2'\|}\right) \tag{9}$$

The angular deviation is defined as $\Delta\theta = |\theta' - \theta_{\text{CAD}}|$, where θ_{CAD} is the theoretical angle in the CAD model. If $\Delta\theta$ is smaller than a predefined threshold, the reconstructed model is considered to preserve the designed angular relationship.

For coplanarity and horizontality verification, the average elevation of points on each line is calculated. Let the point set on line L_k be $\{P_{k,i}\}$. The average elevation is:

$$\bar{Z}_k = \frac{1}{n_k}\sum_{i=1}^{n_k} Z_{k,i} \tag{10}$$

If the difference between average elevations $|\bar{Z}_k - \bar{Z}_l|$(for any two distinct lines L_k and L_l) is smaller than the allowable error, and the residuals of all points relative to the average elevation are within the tolerance range, the lines are considered approximately coplanar. A spatial plane can then be fitted to the point sets. Let the plane equation be $ax + by + cz + d = 0$, with normal vector $\mathbf{n}_{\text{plane}} = (a, b, c)$. The angle between this normal and the horizontal normal $\mathbf{n}_{\text{horizontal}} = (0, 0, 1)$ is:

$$\phi = \arccos\left(\frac{|\mathbf{n}_{\text{plane}} \cdot \mathbf{n}_{\text{horizontal}}|}{\|\mathbf{n}_{\text{plane}}\|}\right) \tag{11}$$

If ϕ is smaller than a preset threshold, the plane is considered parallel to the ground.

If all evaluation indices fall within the predefined tolerance ranges, the 3D reconstruction model is considered to have good consistency with the CAD design model in terms of the macroscopic geometric framework, and the geometric accuracy of the ship component is considered to meet the quality inspection requirements.

3. Experiment

3.1 Experimental Setup

This experiment uses a segmented ship component as the measurement object to verify the feasibility of nap-of-the-object photogrammetry for geometric quality inspection. Figure 8 shows a photograph of the component.

Figure 8. Photograph of the segmented ship component

Data acquisition was performed simultaneously using two DJI Mavic 3E UAVs. In windless conditions, the device has a maximum horizontal flight speed of 15 m/s, a maximum flight time of 45 minutes per sortie, and a maximum range of 32 km. Its integrated wide-angle mapping camera has a field of view of 84°, an equivalent focal length of 24 mm, and a maximum resolution of 5280 × 3956 pixels (approximately 20 megapixels), equipped with a mechanical shutter ranging from 1/2000 s to 8 s to ensure geometric accuracy during dynamic capture. The built-in high-precision GNSS RTK module provides positioning accuracy of 1 cm + 1 ppm horizontally and 1.5 cm + 1 ppm vertically under fixed solution conditions, offering accurate georeferencing for the aerial images.

To verify the applicability of nap-of-the-object photogrammetry to ship component geometric quality inspection, flight path planning is first performed based on the CAD model of the component. Images are then acquired, and photogrammetric processing is performed to reconstruct a high-precision 3D model. Finally, a quantitative assessment of the technical accuracy is performed by comparing the nap-of-the-object photogrammetry model with the CAD design model.

3.2 Flight Path Planning Results

Based on the bounding box of the CAD design model, the ship component is divided into six surface objects, with flight path planning performed for each surface as described in Section 2.1. The flight distance is set to 3–5 m, and the shooting angles are set to frontal and left–right convergent views to ensure full coverage without blind spots. Flight path inspection and simulation are then carried out. After confirming that the flight path poses no collision risk, the flight path file is exported. The flight path planning results for each surface are shown in Figure 9, and the overall flight path is presented in Figure 10.

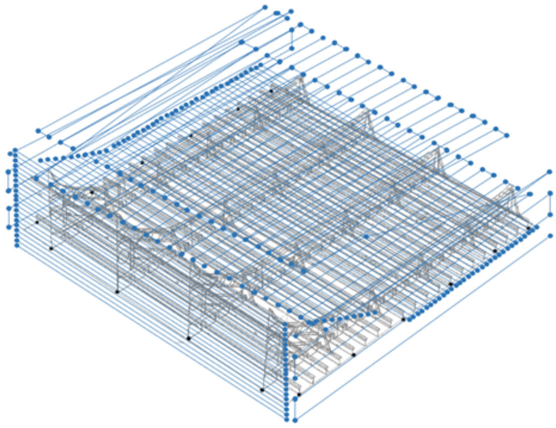

Figure 9. Nap-of-the-object flight path planning for the ship component

After the flight path file is imported into the flight control software, the UAV automatically performs the nap-of-the-object flight. Field data acquisition lasted a total of five hours, yielding 8,851 images. Figure 10 shows some of the captured images.

Figure 10. Selected images of the ship component

3.3 3D Reconstruction Results

For this experiment, eight control points and six checkpoints were selected. The layout of the control points is shown in Figure 11(a), and the orientation accuracy of the control points is presented in Table **??**. The layout of the checkpoints is shown in Figure 11(b), and their orientation accuracy is presented in Table **??**.

Point	dX	dY	dZ
1	0.0022	0.0044	0.0195
2	0.0009	-0.0014	0.0088
3	0.0176	0.0056	0.0261
4	0.0049	0.0030	0.0049
5	0.0676	-0.0462	0.0181
6	0.0015	-0.0174	-0.0003
7	-0.0079	-0.0030	0.0037
8	0.0702	-0.0396	-0.0010
RMS: X: 0.0300, Y: 0.0192, Z: 0.0094			

Table 1. Accuracy of control points (Unit: m)

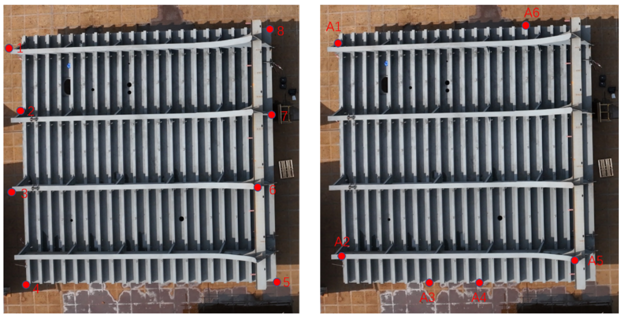

(a) (b)

Figure 11. (a) Layout of control points, (b) Layout of checkpoints

Point	dX	dY	dZ
1	0.0011	0.0188	0.0052
2	0.0067	0.0000	0.0045
3	0.0028	0.0062	0.0069
4	0.0000	0.0042	0.0085
5	0.0079	0.0625	0.0237
6	0.0016	0.0000	0.0004
RMS: X: 0.0029, Y: 0.0220, Z: 0.0074			

Table 2. Accuracy of checkpoints (Unit: m)

Using 3D reconstruction technology, images acquired through nap-of-the-object photogrammetry were processed to generate a nap-of-the-object 3D model, as shown in Figure 12. The 3D model does not have holes or stretched texture, and the texture is clear.

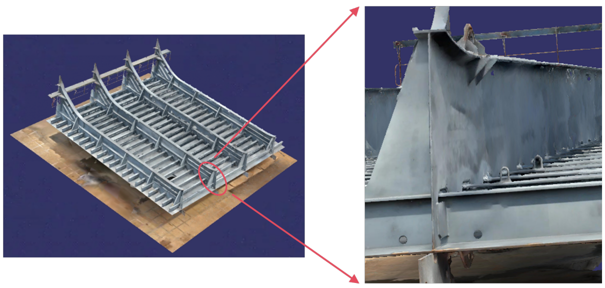

Figure 12. Nap-of-the-object 3D model

3.4 Geometric Quality Inspection Results

To evaluate whether the measurement method based on nap-of-the-object photogrammetry meets the accuracy requirements for ship component quality inspection, points along the weld edges of the steel plates were selected as measurement points, following the principles of overall uniformity and distinct geometric features, as shown in Figure 13. Key points measured in the 3D reconstruction model were subjected to line fitting, and the geometric relationships were compared with those in the CAD design model. Table **??** presents the differences between the design values from the CAD model and the measured values from the 3D reconstruction model.

The fitting results indicate that the 3D reconstruction model maintains the geometric relationships well. In terms of angular deviation, the inter-edge angle deviations between surfaces 1 and 2, and between surfaces 1 and 3, are both less than 0.05°, falling within the predefined tolerance range, demonstrating that the reconstructed model maintains high consistency with the CAD

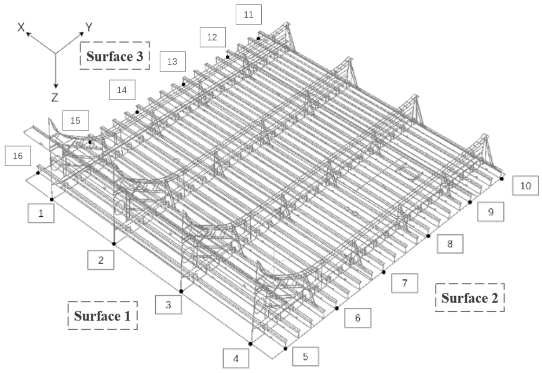

Figure 13. Measurement point layout in the CAD design model

Point	dx	dy	dz
1	0.007	0.018	-0.003
2	0.002	0.019	-0.002
3	0.004	0.020	0.001
4	0.003	0.019	-0.001
5	-0.004	0.001	0.003
6	-0.003	0.005	0.001
7	-0.005	0.003	0.001
8	-0.004	0.005	-0.001
9	-0.002	0.003	0.003
10	-0.004	0.004	0.001
11	0.001	0.004	-0.002
12	-0.001	0.004	0.003
13	-0.001	0.002	0.001
14	-0.001	0.002	0.003
15	0.001	-0.001	0.001
16	0.001	0.002	0.001

Table 3. Errors between CAD model design values and 3D reconstruction model measurements (Unit: m)

design in terms of perpendicularity. The parallelism deviation between surfaces 2 and 3 is less than 0.02°, further confirming that these surfaces maintain a good parallel relationship in the production of the ship component.

Regarding coplanarity and horizontality, Table **??** shows that the Z-direction errors at all measured points are within ±5 mm, with no significant systematic drift. The average elevations of points on the three edges were calculated, and the maximum difference was less than 5 mm, indicating that the three edges remain essentially coplanar after reconstruction. The plane fitted from these points and the angle between its normal vector and the vertical direction were within the allowable range, confirming that the reconstructed model exhibits good consistency with the CAD design model in terms of the macroscopic geometric framework.

The geometric accuracy verification results based on geometric primitive fitting indicate that the 3D reconstruction model meets the quality inspection requirements for macroscopic geometric indicators such as perpendicularity, parallelism, and coplanarity.

After confirming these indicators, distance measurements were performed on the nap-of-the-object 3D model using the points marked in Figure 13. Each distance was measured twice: Measurement 1 from right to left, and Measurement 2 from left to right. The measured distances were compared with the CAD design values, and the results are presented in Tables **??**–**??**.

As shown in Tables **??**–**??**, most differences between the model-measured distances and the CAD design distances are within ±5

Point Pair	CAD design value	Measurement 1		Measurement 2	
		Measured	Error	Measured	Error
1–2	4.3650	4.3658	0.0008	4.3610	-0.0040
2–3	4.3580	4.3608	0.0028	4.3614	0.0034
3–4	4.3610	4.3645	0.0035	4.3622	0.0012
1–4	13.0840	13.0859	0.0019	13.0792	-0.0048

Table 4. Errors between nap-of-the-object 3D model distance measurements and CAD design values: Surface 1 (Unit: m)

Point Pair	CAD design value	Measurement 1		Measurement 2	
		Measured	Error	Measured	Error
5–6	3.2868	3.2843	-0.0025	3.2855	-0.0013
6–7	3.2808	3.2855	0.0047	3.2832	0.0024
7–8	3.2848	3.2876	0.0028	3.2852	0.0004
8–9	3.2806	3.2833	0.0027	3.2849	0.0043
9–10	2.4632	2.4486	-0.0146	2.4506	-0.0126
5–10	15.5961	15.5919	-0.0042	15.5856	-0.0105

Table 5. Errors between nap-of-the-object 3D model distance measurements and CAD design values: Surface 2 (Unit: m)

Point Pair	CAD design value	Measurement 1		Measurement 2	
		Measured	Error	Measured	Error
11–12	2.4622	2.4593	-0.0029	2.4607	-0.0015
12–13	3.2846	3.2891	0.0045	3.2894	0.0048
13–14	3.2829	3.2781	-0.0048	3.2798	-0.0031
14–15	3.2857	3.2849	-0.0008	3.2854	-0.0003
15–16	3.2797	3.2791	-0.0006	3.2802	0.0005

Table 6. Errors between nap-of-the-object 3D model distance measurements and CAD design values: Surface 3 (Unit: m)

mm. The distance error between points 9 and 10 on Surface 2 exceeds 1 cm, primarily due to irregularities in the model at point 10, as illustrated in Figure 14. Overall, the measurements based on nap-of-the-object photogrammetry are in close agreement with the CAD design model.

In summary, the geometric accuracy verification results based on geometric primitive fitting indicate that the 3D reconstruction model meets the quality inspection requirements for perpendicularity, parallelism, coplanarity, and detailed spacing. Therefore, in practical production, nap-of-the-object photogrammetry can be used for rapid, non-contact geometric quality inspection of ship components, providing an efficient and feasible technical solution for ship manufacturing.

4. Conclusion

Nap-of-the-object photogrammetry is applied to ship component measurement in this paper. First, flight path planning is performed based on the CAD design model of the ship component, and high-resolution images are acquired using a UAV. Exterior orientation parameters such as heading, attitude, and gimbal angle are then integrated to generate a high-precision 3D reconstruction model. Finally, quality inspection is carried out by comparing the measurement results from the 3D reconstruction model with the CAD design model. Key point coordinates and bidirectional point distances corresponding to those in the CAD model are measured on the 3D reconstruction model, and straight lines representing key geometric features are fitted to evaluate the perpendicularity and coplanarity of ship component details, thereby enabling an assessment of geometric accuracy.

A segmented ship component was selected for experimental validation. The results show that the distance measurements based on the nap-of-the-object 3D model differ from the CAD design values by within 5 mm in most cases, with a maximum error

Figure 14. Point 10 on the nap-of-the-object 3D model

of 1.46 cm, indicating that nap-of-the-object photogrammetry provides reliable results for ship component quality inspection. In addition, this method offers non-contact operation, high precision, and high efficiency, which can significantly improve production efficiency in the shipbuilding industry and promote its modernization.

References

Ahmed, G., Sheltami, T., Mahmoud, A., 2024. Energy-efficient multi-UAV multi-region coverage path planning approach. *Arabian Journal for Science and Engineering*, 49(9), 13185–13202.

Bao, Z., Zhang, Z., Xie, C., 2023. Landmark selection and path planning for unmanned vehicles with position error corrections. *Transportation research part C: emerging technologies*, 153, 104186.

Chai, X., Zheng, Z., Xiao, J., Yan, L., Qu, B., Wen, P., Wang, H., Zhou, Y., Sun, H., 2022. Multi-strategy fusion differential evolution algorithm for UAV path planning in complex environment. *Aerospace Science and Technology*, 121, 107287.

Chen, Y., Liu, X., Zhu, B., Zhu, D., Zuo, X., Li, Q., 2025. UAV Image-Based 3D Reconstruction Technology in Landslide Disasters: A Review. *Remote Sensing*, 17(17), 3117.

Dujam, M., Stojaković, A., Hadjina, M., Legović, D., Turk, A., 2024. Comparison of the Classic Method of Hull Shape Assessment of a 5-Meter L5 Sailboat with the Photogrammetry Method. *Pomorski zbornik*, 193–211.

Faizin, M., Paryanto, P., Cahyo, N., Rusnaldy, R., 2024. Investigating the accuracy of boat propeller blade components with reverse engineering approach using photogrammetry method. *Results in Engineering*, 22, 102293.

Iglhaut, J., Cabo, C., Puliti, S., Piermattei, L., O'Connor, J., Rosette, J., 2019. Structure from motion photogrammetry in forestry: A review. *Current Forestry Reports*, 5(3), 155–168.

Jones, M., Djahel, S., Welsh, K., 2023. Path-Planning for Unmanned Aerial Vehicles with Environment Complexity Considerations: A Survey. *ACM Comput. Surv.*, 55(11). https://doi.org/10.1145/3570723.

Kim, J., Lee, J., Park, Y.-H., 2024. Highly accurate three-dimensional measurement of large structures using multiple stereo vision with improved two-step calibration algorithm. *Measurement*, 234, 114886.

Li, C., Chen, L., Xiao, Y., Wang, J., 2022. Experiment on accuracy of image-based 3d reconstruction for large construction site with cors network rtk. *2022 4th International Conference on Frontiers Technology of Information and Computer (ICFTIC)*, 160–165.

Li, J., Chen, Z., Lei, P., Li, D., Yi, J., 2025. Construction accuracy evaluation of ship stiffened panel based on 3D model reconstruction. *Ocean Engineering*, 328, 121060.

Liu, T., Shen, R., Lei, Z., Huo, Y., Zhao, J., Xu, X., 2022. Wind resistance aerial path planning for efficient reconstruction of offshore ship. *International Journal of Digital Earth*, 15(1), 1881–1904.

Maisano, D. A., Mastrogiacomo, L., Franceschini, F., Capizzi, S., Pischedda, G., Laurenza, D., Gomiero, G., Manca, G., 2023. Dimensional measurements in the shipbuilding industry: on-site comparison of a state-of-the-art laser tracker, total station and laser scanner. *Production Engineering*, 17(3), 625–642.

Niebylski, J., 2025. Photogrammetric methods of measurement during building of ships. *WIT Transactions on The Built Environment*, 27.

Rodríguez-Lira, D.-C., Córdova-Esparza, D.-M., Terven, J., Romero-González, J.-A., Alvarez-Alvarado, J. M., González-Barbosa, J.-J., Ramírez-Pedraza, A., 2025. Recent developments in image-based 3D reconstruction using deep learning: Methodologies and applications. *Electronics*, 14(15), 3032.

Son, Y.-B., Nam, J.-H., 2022. Creation of hierarchical structure for computerized ship block model based on interconnection relationship of structural members and shipyard environment. *International Journal of Naval Architecture and Ocean Engineering*, 14, 100455.

Wang, Y., Feng, H.-Y., 2016. Effects of scanning orientation on outlier formation in 3D laser scanning of reflective surfaces. *Optics and Lasers in Engineering*, 81, 35–45.

Yuzaki, M., Okomoto, Y., 1993. An Approach to a New Ship Production System Based on Advanced Accuracy Control. *Journal of Ship Production*, 9(02), 113-120.

Zhang, W., Li, J., Yu, W., Ding, P., Wang, J., Zhang, X., 2024. Algorithm for UAV path planning in high obstacle density environments: RFA-star. *Frontiers in Plant Science*, 15, 1391628.

Zhong, Y., Xue, K., Shi, D., 2013. Assembly unit partitioning for hull structure in shipbuilding. *Computer-Aided Design*, 45(12), 1630–1638.